Review

Carbon Future

Activation and transformation of carbon dioxide by gas-phase species: Mechanisms and advances

Chuman Sun, Fengxiang Zhang, Xiaowang Li, and Jiabi Ma

Key Laboratory of Cluster Science of Ministry of Education, Beijing Key Laboratory of Photoelectronic/Electrophotonic Conversion Materials, School of Chemistry and Chemical Engineering, Beijing Institute of Technology, Beijing 102488, China

Cite This: *Carbon Future* **2026**, *3*, 9200076

Read Online

ABSTRACT: CO_2 activation and transformation processes are essential for sustainable energy development and environmental remediation. In this review, we describe our advances in the use of gas-phase ions to mediate these processes, which have provided unique molecular-level mechanistic insights by combining mass spectrometry and density functional theory calculations. This review is structured around three fundamental CO_2 transformation reactions: reduction to CO through O-atom transfer to a suitable oxygen acceptor, B–C bond formation via reactions with metal borides, and C–N bond formation via coupling with NH_3 or N_2. The fundamental knowledge uncovered in these gas-phase studies establishes a foundational framework for future research and the rational design of novel catalytic systems for CO_2 conversion.

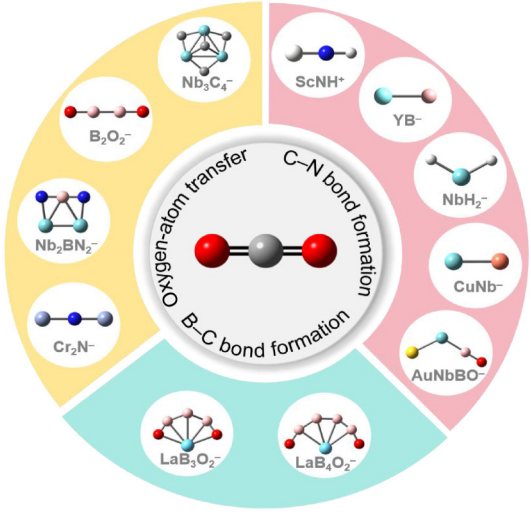

KEYWORDS: carbon dioxide activation, mass spectrometry, theoretical calculations, gas-phase chemistry

1 Introduction

Excessive CO_2 emissions, primarily caused by fossil fuel combustion, transportation, and industrial activities, have become a major contributor to the greenhouse effect and global climate change[1–3]. In response, China has introduced the dual-carbon policy, aiming to achieve carbon peaking and carbon neutrality, with the long-term goal of net-zero CO_2 emissions by 2050. Against this backdrop, balancing CO_2 emissions and consumption has emerged as a critical global challenge. One promising approach is the catalytic conversion of CO_2 into valuable chemical materials, which represents a sustainable pathway toward environmental protection and carbon resource utilization[4]. Remarkable progress has been made in this direction, enabling the transformation of CO_2 into various products, such as CO, CH_4, C_2H_4, C_2H_5OH, acetic acid, acetate, acetone, acetaldehyde, and propanol, via diverse catalytic strategies, including electrochemical[5], photochemical[6], thermochemical[7], plasma-assisted[8], and radiocatalytic methods[9]. In the electrocatalytic and thermocatalytic reduction of CO_2, once CO_2 is adsorbed onto the active site, the primary electron transfer event generates a surface-adsorbed carbonate radical intermediate ($*CO_2^-$)[10]. The isolated O atom of the CO_2 molecule is extremely sensitive to the attack of *H, thereby forming the intermediate product *COOH. This intermediate can rapidly undergo proton-coupled electron transfer via an electrophilic addition–elimination mechanism or alternatively proceed toward *CO, with this process affecting the C_1/C_2 selectivity in the downstream products[11, 12]. Commonly, *COOH is more likely to form C_1-type intermediate products via further hydrogenation pathways, such as *CHO, *COH, and $*CH_2$, which then transform into formic acid, CH_4, or CO. In contrast, *CO can initiate C–C coupling via self-coupling or interaction with other surface-adsorbed substances such as *CHO, *COH, and $*CH_2$, thereby generating multicarbon (C_2+) products[13]. Despite considerable efforts, precisely identifying the active sites and understanding the reaction mechanisms at the molecular level[14], which is essential for the rational design of high-performance catalysts, remains as a fundamental challenge.

Received: December 29, 2025; **Revised:** March 17, 2026
Accepted: April 3, 2026

Address correspondence to Jiabi Ma, majiabi@bit.edu.cn

https://doi.org/10.26599/CF.2026.9200076

Gas-phase studies on isolated atomic clusters have long been considered ideal for probing reaction mechanisms relevant to condensed-phase systems under controlled, reproducible conditions. Investigations of the reactivity of atomic clusters with small molecules allow examining individual active sites at the molecular level without the complexities of condensed-phase systems, such as aggregation and solvent effects. Although gas-phase models cannot fully replicate the condensed-phase small molecules conversion, they yield molecular-level insights into crucial issues, including elementary steps, reactive intermediates, doping effects, and ligand effects[15–25]. Thus, gas-phase cluster studies provide essential mechanistic insights complementary to condensed-phase investigations. In this collaborative work, we employed mass spectrometry–based gas-phase cluster experiments to elucidate the molecular-level mechanism of CH_3OH-mediated Cu migration[26], finding that the reaction of gas-phase Cu_2^+ clusters with CH_3OH vapor produces Cu^+, thereby supporting the reverse ripening of Cu nanoparticles. In the context of CO_2 activation, numerous gas-phase metal species, including bare metal ions, metal oxides, and metal hydrides, have been reported[19, 20, 27–29]. The work on CO_2 activation prior to 2021 is summarized in detail in a review by He[20]. Recent advances on CO_2 conversion include the gas-phase cluster-catalyzed CO_2 reduction to CO by $CoCD_n^-$[30] and $RhTaC_2^-$[31]. In the co-conversion reaction of CH_4 and CO_2, the heteronuclear metal oxide clusters $RhTiO_2^-$[32] and Rh_2CoO^-[33] facilitate the H_2 and CO, the heteronuclear metal cation $CuTa^+$ promotes the C_2 products ($H_2C{=}C{=}O$)[34], and the homonuclear metal oxide $Ta_2O_2^+$ produces acetylene ($CH{\equiv}CH$) via CH_4–CO_2 coupling[35]. Mechanistic aspects of the reactions of various gas-phase metal species with CO_2 have been extensively investigated by Schwarz[19].

In this review, we focus on our investigation of the mechanisms by which gas-phase metal-containing species react with CO_2 using mass spectrometry combined with density functional theory (DFT) calculations. From a mechanistic point of view, we categorize CO_2 transformations into three fundamental pathways: reduction to CO via O-atom transfer (OAT), B–C bond formation through reactions with metal borides, and C–N bond formation via coupling with NH_3 or N_2.

2 Reduction of CO_2 to CO via oxygen-atom transfer

The reduction of CO_2 to CO via OAT is the most prevalent reaction pathway for CO_2 conversion. Its feasibility is primarily determined by thermodynamics: the O atom affinity of the clusters must exceed the bond energy of the C=O bond in CO_2[19, 36]. This principle was clearly demonstrated in 2006 by Bohme's group, who evaluated the reactivity of CO_2 with 46 atomic cations using an inductively coupled plasma–selected-ion flow tube tandem mass spectrometer, identifying only nine atomic cations (Sc^+, Y^+, La^+, Ti^+, Zr^+, Hf^+, Nb^+, Ta^+, and W^+) that fulfill this criterion and promote the CO_2 reduction to CO. The scope of OAT-mediated CO_2 reduction has extended far beyond atomic metal ions to include various gas-phase clusters, such as metal oxides, hydrides, nitrides, carbides, and borides. Representative examples are compiled in **Table 1**.

Table 1 Summary of CO_2 reduction to CO via O-atom transfer with various gas-phase metal-containing clusters

Cluster	Ionic product	Neutral product	Year	Ref.
Ta^{2+}	TaO^{2+}	CO	2012	[37]
V_2^+; V_2O^+	V_2O^+; $V_2O_2^+$	CO	2020	[38]
UO^+	UO_2^+	CO	1980	[39]
NbO^+	NbO_2^+, $NbCO_2^+$	CO, O	1998	[40]
PtO^+	Pt^+, PtO_2^+, $PtCO_2^+$	$O + CO_2$, $O_2 + CO$, CO, O	2003	[41]
ReO_2^-	ReO_3^-	CO	2016	[42]
FeH^-	HCO^-, $HFeO^-$, FeO_2H^-	Fe, CO	2017	[43]
CoH^-	$HCoO^-$	CO	2020	[43]
NiH^-	$NiOH^-$	CO	2020	[44]
Cr_xN^- (x = 2–7); Cr_2NH^-	$Cr_xNO_2^-$; Cr_2NHO^-	CO	2020	[45][a]
$Nb_3C_4^-$	$Nb_3C_4O_{1-5}^-$	CO	2024	[46][a]
$TaCH_2^+$	$TaOCH_2^+$, TaO_2^+	CO, C_2H_2O	1995	[47]
$[HTaO]^+$; $[TaOH]^+$	$[OTaOH]^+$	CO	2016	[48]
$Nb_2N_2^-$ Nb_2B^- $Nb_2BN_2^-$	$Nb_2N_2O_{1-2}^-$ $Nb_2BO_{1-3}^-$ $Nb_2BN_2O_{1-4}^-$	CO	2020	[49][a]
$[Re(CO)_2]^+$	$[Re(CO)_2O]^+$	CO	2017	[50]
$Mo_xW_yO_z^-$	$Mo_xW_yO_{z+1}^-$, $Mo_xW_yO_{z+2}C^-$	CO	2010	[51]
$RhVO_3CH_4^-$	$RhVO_3HCO_2^-$, $RhVO_3CH_2O^-$, $RhVO_3CO^-$, $RhVO_3CH_4O^-$	CH_3, CH_2O, CH_3OH, CO	2019	[52]
$Rh_2VO_2CH_2^-$	$Rh_2VO_2C^-$, $Rh_2VO_{z-1}^-$	H_2, H_2 + CO	2020	[53]
$[LTiH]^+$ (L = Cp_2, O)	$[OTi(OH)]^+$, $[Cp_2Ti(O_2CH)]^+$	CO	2015	[54]
$B_2O_2^-$	$B_2O_{3-4}^-$	CO	2023	[55][a]

[a]These clusters were reported by our research group.

Carbon Future

Extensive research has been devoted to the activation and conversion of CO_2 mediated by Nb-based catalysts[49, 56–58]. Early studies, such as the ion beam mass spectrometry–guided investigation of Nb^+ reactions with CO_2 reported in 1998, demonstrated that Nb^+ reacts with CO_2 to form NbO^+ and CO[40]. Concurrently, the choice of appropriate ligands is essential for activating small molecules. For instance, NbO^+ has been shown to convert CO_2 into CO[59]. Recently, we explored the thermal gas-phase reactions of $Nb_2N_2^-$, Nb_2B^-, and $Nb_2BN_2^-$ with CO_2 using time-of-flight mass spectrometry and DFT calculations[49]. Interestingly, unlike NbO^+, the $Nb_2N_2^-$, Nb_2B^-, and $Nb_2BN_2^-$ clusters can sequentially reduce multiple CO_2 molecules. Specifically, $Nb_2N_2^-$ reduces two CO_2 molecules and Nb_2B^- reduces three, yielding $Nb_2N_2O_{1-2}^-$, and $Nb_2BO_{1-3}^-$, respectively, while releasing CO in each step. Notably, $Nb_2BN_2^-$ exhibits even higher reactivity, reducing up to four CO_2 molecules to generate $Nb_2BN_2O_{1-4}^-$, again releasing one CO molecule per reduction step. **Scheme 1** illustrates the reaction pathways of $Nb_2N_2^-$, Nb_2B^-, and $Nb_2BN_2^-$ with CO_2. In the case of $Nb_2N_2^-$, two CO_2 molecules are successively adsorbed and activated at different Nb sites, generating $Nb_2N_2O_2^-$ and two CO molecules. The reaction of Nb_2B^- with CO_2 involves two coordination modes. In one mode, the C atom of a CO_2 molecule coordinates with two Nb atoms, and the C atom of another CO_2 molecule coordinates with one Nb atom and the B atom. The other coordination mode exhibits the opposite configuration. In a separate process, the C atom of a third in CO_2 is reduced while it coordinates to one Nb atom and the B atom in a similar fashion. Thus, three CO_2 molecules are successfully reduced in this system, releasing three CO molecules and generating $Nb_2BO_3^-$. In the reaction of $Nb_2BN_2^-$ with CO_2, two Nb atoms work synergistically to adsorb and activate two CO_2 molecules, with the third and fourth CO_2 molecules being adsorbed and activated at the same Nb site. The high catalytic activity of $Nb_2BN_2^-$ is closely related to the presence of the B atom, which not only remarkably shortens the Nb–Nb bond length, thereby facilitating the storage of electrons in the Nb–Nb bond for the following CO_2 reduction reactions, but also provides its empty orbital, which is equivalent to the d orbital of transition metals, as an electron donor. This work demonstrates that a transition metal (Nb) and a main-group atom (B) can work synergistically to reduce CO_2. The observed reactivity of $Nb_2BN_2^-$ with CO_2 provides molecular-level insights that can be exploited to develop efficient active sites on supported transition metal/BN materials for CO_2 activation and transformation.

To activate a greater number of CO_2 molecules, we extended our study to niobium carbide anions $Nb_3C_{1-4}^-$. Among $Nb_3C_{1-4}^-$ anions, $Nb_3C_4^-$, which carries the maximum number of C ligands, exhibits the highest reactivity, being capable of reducing up to five CO_2 molecules[46]. It is noteworthy that all five reaction pathways share several common features, as briefly summarized in Fig. 1a. A consistent trend across all pathways is the initial capture of a CO_2 molecule at the Nb–C^a site, which results in the formation of a four-membered ring structure. In this initial step, a partial electron (about 0.5*e*–0.7*e*) transfers to CO_2, activating the C=O double bonds in CO_2. Cleavage of the first C=O bond generates an OCC^a unit containing one C=C bond. Subsequently, the reaction diverges into two distinct pathways. Pathway A represents the pattern for the reaction of $Nb_3C_4O^-$ with CO_2, where a CO unit is directly removed by breaking the C=C bond. Meanwhile, pathway B explains the reactions of $Nb_3C_4^-$ and $Nb_3CO_{2-4}^-$ with CO_2. After breaking the first C=O bond, CO cannot evaporate directly owing to the high energy barriers. Instead, the OCC^a unit interacts with another C atom to form a new C^a–C^b bond. Structural rearrangement then shortens the bond length of C^a=C^b, facilitating subsequent CO evaporation.

The mass spectrometry results of this study revealed a distinct size-dependent reactivity of the $Nb_3C_{1-4}^-$ cluster toward CO_2. As

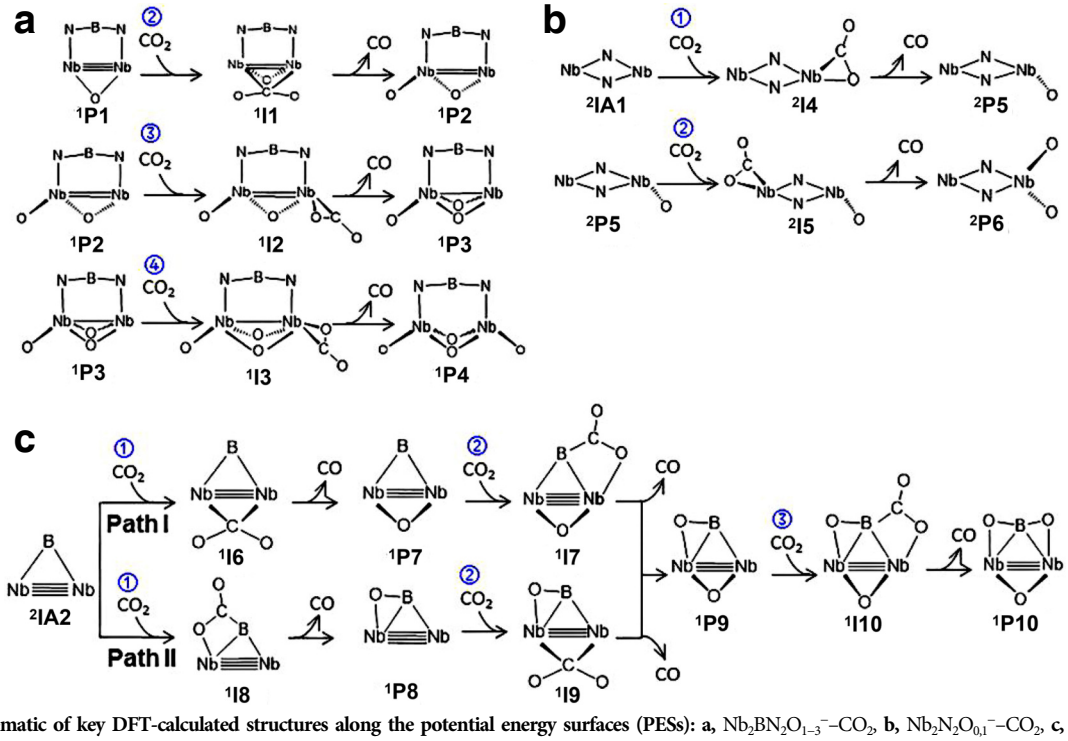

Scheme 1. Schematic of key DFT-calculated structures along the potential energy surfaces (PESs): a, $Nb_2BN_2O_{1-3}^-$–CO_2, **b,** $Nb_2N_2O_{0,1}^-$–CO_2, **c,** $Nb_2BO_{0-2}^-$–CO_2 systems. The superscripts denote the spin multiplicities. Reproduced with permission from Ref.[49], © The Royal Society of Chemistry 2020.

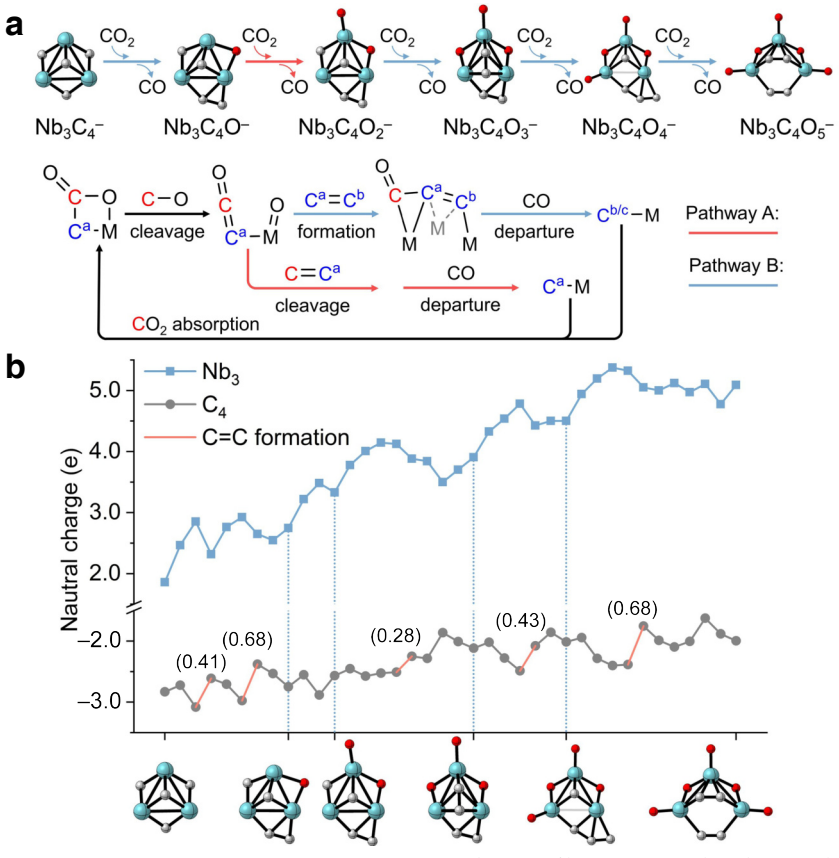

Fig. 1. Schematic illustration of the reaction mechanisms and charge distribution. a, Schematic of key processes and mechanisms along the PESs for the reactions of $Nb_3C_4O_{0-4}^-$ with CO_2. **b,** Total natural charges on the three Nb atoms and four C atoms. The red lines indicate five C–C coupling processes, and the numbers of charges released by C atoms are given within brackets. The M06 functional is given. The aug-cc-pVTZ basis set was selected for C and O atoms, and the def2-TZVPD basis set was selected for the Nb atom. Reproduced with permission from Ref.[46], © American Chemical Society 2024.

the number of C atoms increases, the three Nb–Nb bond lengths increase obviously, indicating electron transfer from the Nb–Nb bonds to either Nb–C or C–C bonds, as depicted in Fig. 1b. In these five reaction systems, the Nb atom serves as the primary electron donor. Meanwhile, the C ligands act as electronic storage reservoirs, allowing the stored electrons to be released effectively through these five C–C coupling reactions. Compared with pure metals, transition-metal carbides are considered promising industrial catalysts owing to their superior selectivity, durability, and stability[60,61]. It is widely recognized that incorporating C atoms into transition-metal lattices modifies their electronic properties and crystalline structures. In contrast with the previously reported $Nb_2BN_2^-$[49] and $RhTaC_2^-$[31] clusters, $Nb_3C_4^-$ activates CO_2 via a distinct electron transfer pathway, demonstrating consistent reactivity and enhanced catalytic performance. Experimental and theoretical findings highlight the essential role of C ligands at the transition-metal–C active sites. We anticipate that precise control over the number of C atoms will enable the design of transition-metal carbides with both high activity and selectivity.

As a main-group element, B exhibits a unique combination of lone electron pairs and vacant orbitals, enabling it to mimic transition metals in various reactions[62]. We reported that the metal-free cluster $B_2O_2^-$ can successively activate two CO_2 molecules, generating $B_2O_{3,4}^-$ and two CO molecules[55]. This reactivity stems from the tendency of B to form multicenter bonds involving its unoccupied 2p orbital. The adaptive natural density partitioning bonding analysis shown in **Fig. 2a** reveals a B≡O bond in $B_2O_2^-$, which originates from two 2c–2e σ bonds and four 2c–2e π bonds between B and O_t atoms. $B_2O_4^-$ exhibits six 2c–2e B–O_t σ bonds and two 2c–2e B–O_t π bonds with a B–O bond length of 144 pm, consistent with a double bond. These results suggest that the B≡O bond in boron oxide anions is destabilized during CO_2 activation. In addition, the two-dimensional electron localization function (ELF) analysis in Fig. 2b shows a notable reduction in electron density between the two B atoms in $B_2O_4^-$, confirming their role as electron donors. CO_2 reduction conducted by these metal-free ions differs from that involving their transition metal equivalents in that in the latter, the transition metal itself or its combination with ligands usually provide electrons, whereas B atoms act as the electron donors in the former (Fig. 2c). Typically, an O atom from CO_2 first transfers to the transition-metal atom, followed by the release of CO from the metal center. However, in the $B_2O_2^-$–CO_2 system, the two C–O bonds are not fully cleaved prior to product formation, resulting in the direct release of CO from the CO_2 component itself. Such a mechanistic understanding of the fundamental steps will be valuable for catalyst optimization.

Furthermore, we systematically investigated CO_2 activation and conversion mediated by a series of chromium nitride clusters in the gas phase[45]. Under thermal collision conditions, Cr_xN^- clusters (x = 2–7) can successively reduce two CO_2 molecules to generate two CO molecules. As shown in **Fig. 3**, the reactivity of Cr_xN^- first increases and then slightly decreases as the number of Cr atoms rises from 2 to 7. Notably, Cr_2NH^- can also activate one CO_2 molecule to produce Cr_2NHO^- and one CO molecule. These

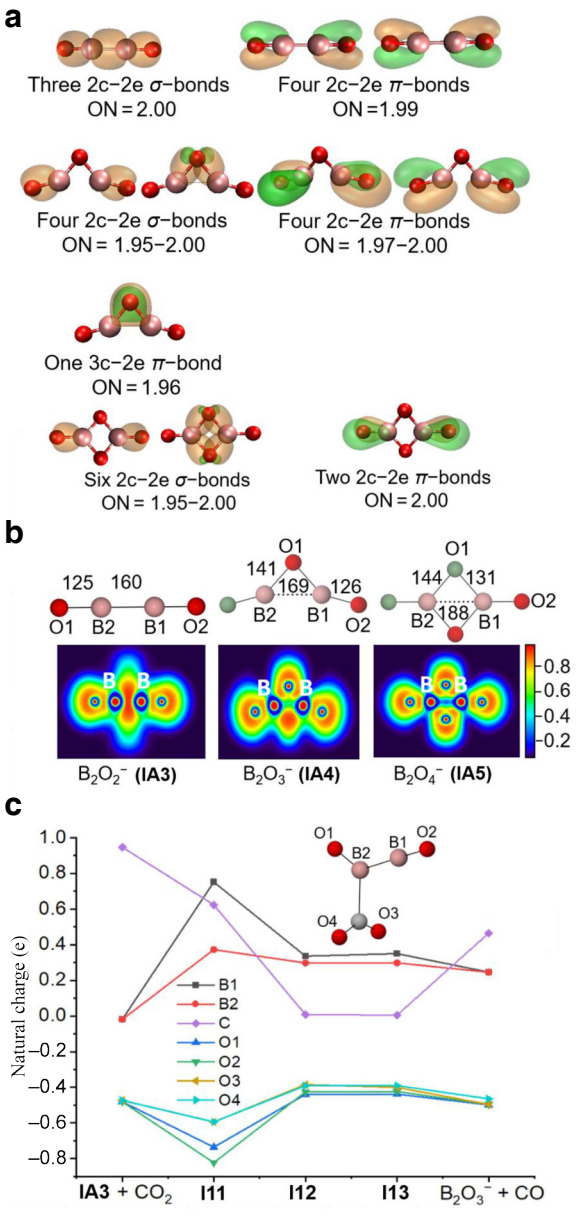

Fig. 2. Bonding analysis and natural charges. a, Adaptive natural density partitioning bonding analysis for $B_2O_{2-4}^-$. ON stands for the occupation number (2c–2e and 3c–2e bonds). **b,** Electron localization function (ELF) analysis of $B_2O_{2-4}^-$. A large ELF value means that electrons are greatly localized. **c,** Calculated natural charges along the reaction coordinates of CO_2 activation on $B_2O_2^-$ clusters. The TPSS functional, including the DFT-D3 dispersion correction, is given. The 6-311+G* basis set was selected for C and O atoms, and the aug-ccPVTZ basis set was selected for the B atom. Reproduced with permission from Ref.[55], © American Chemical Society 2023.

reactions share several common features: (i) The formation of an adsorption intermediate, in which an O atom from CO_2 coordinates to a Cr atom, releases substantial energy (> 1.5 eV). Accompanying this step, electron transfer from the cluster to CO_2 induces a bent O–C–O configuration. (ii) The activation barrier for the OAT process remains relatively constant (approximately 0.5 eV), except for the first transition state in the reaction path between Cr_4NO^- and CO_2. (iii) In the first CO_2 reduction step, the release of the newly generated CO unit from the $[Cr_xNO^-\cdots CO]$ intermediate is likely the rate-determining step; in the second CO_2

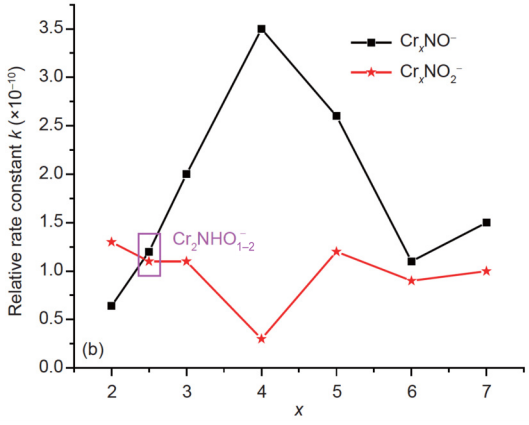

Fig. 3. Absolute rate constants (k_1) of the reaction of Cr_xN^- with CO_2, where *x* represents the number of Cr atoms. Reproduced with permission from Ref.[45].

reduction, the transformation beyond the transition state is the rate-limiting step. As the number of Cr atoms increases, the coordination number of Cr rises. However, the increased size generates potential desorption sites for CO molecules, thereby facilitating their release (Fig. 3). This study represents the first example of multinuclear transition-metal nitride cluster anions mediating CO_2 activation and conversion in gas-phase cluster chemistry.

3 Coupling processes leading to B–C bonds

The formation of B–C bonds is relevant for the synthesis of diverse organoboron compounds. In the condensed phase, the predominant synthetic strategy for producing organoboron compounds is the transition metal–catalyzed (Ir, Cu, Rh, and Pd) direct borylation of hydrocarbons via C–H bond activation[63, 64], with carbene insertion into B–H bonds representing another viable pathway[65, 66]. A major limitation of these approaches is that they require high-temperature conditions, which contradicts the tenets of sustainable development.

In gas-phase studies, there are several methods to construct B–C bonds. The matrix isolation method at 4–45 K, using CO[67–74] and organic compounds (CS_2, CH_2=CH_2, CH≡CH, C_6H_6, or acetonitrile) as carbon feedstocks[75–79]; Wang et al. found a series of compounds possessing B–C bonds, such as CB_9^- and $C_2B_8^-$ at 298 K[80, 81]; Yang et al. synthesized $B_4(CO)_3$ by mixing B and CO at 298 K[82]; Zhou et al. also synthesized NNBCO and ONBCO molecules by mixing B, CO, and N_2 or NO at 4–25 K[83, 84]. Constructing the B–C bond is quite an important step in the synthesis of organoboron compounds[85]. **Table 2** summarizes reported methods for B–C bond construction in the gas phase. It is divided into two categories: reactions below 4–45 K[67–74, 83, 84] and reactions at room temperature[80–82, 86–95]. We investigated the gas-phase reactions of a series of lanthanide boron oxide clusters with CO_2 at room temperature[96]. Among them, $LaBO^-$, $LaB_2O_2^-$, $LaB_3O_{3-5}^-$, and $LaB_4O_3^-$ mediate the reduction of CO_2 to CO via OAT (Figs. 4a–4d). Meanwhile, $LaB_3O_2^-$ and $LaB_4O_2^-$ not only reduce CO_2 but also produce novel B–C-bonded species, including $CB_2O_2^-$, $CB_3O_3^-$, and $CB_3O_2^-$. As revealed by structural analyses and ELF calculations (Figs. 4e and 4f), increasing the number of B atoms promotes the formation of B–B and B–La bonds. Concomitantly, electrons initially localized on La and B atoms

Table 2 Reported methods for constructing B–C bonds in the gas phase. Reproduced with permission from Ref.[96], © American Chemical Society 2024

Method	Reactant	Products	Temperature (K)	Ref.
MI-ESR/MI-IR	B–CO	$C_xB_yO_z$	4–45	[67–74]
	B–CO–N_2 (NO)	NNBCO, ONBCO	4–25	[83, 84]
	B–CS_2	$B(CS)_{1,2}$	4–35	[75]
	B–CH_2=CH_2	H_2CBCH_2, $HCBCH_3$	4–12	[76]
	B–CH≡CH	cyclic-HBC_2BH	4–12	[77]
	B–C_6H_6	η^2-(1,4) π adduct	4–12	[78]
	B–CH_3CN	$NCBCH_3$	4–8	[79]
PES	B–C–Cu(Bi)	C_xB_y	298	[80, 86–90]
IR	B–CO	$B_3(CO)_{3-6}^+$	298	[91, 92]
IR + VUV-IS	B–CO	$B_4(CO)_{2,3}$	298	[82]
MS reactions	$B_{12}Br_{11}^-$–CH_4	$[B_{12}Br_{11}CH_3]^{2-}H^+$	298	[93]
	CuB^+–CO_2	CBO_2	298	[94]
	CuB^+–CH_4	$CuBCH_3^+$, CBH_4	298	[94]
	VB^+–CH_4	VCH_2^+, B_3CH_3	298	[95]
TOF-MS	$LaB_mO_n^-$ (m = 1–4, n = 1 or 2)	$CB_2O_2^-$, $CB_3O_3^-$, $CB_3O_2^-$	298	[96][a]

[a]These clusters were reported by our research group.

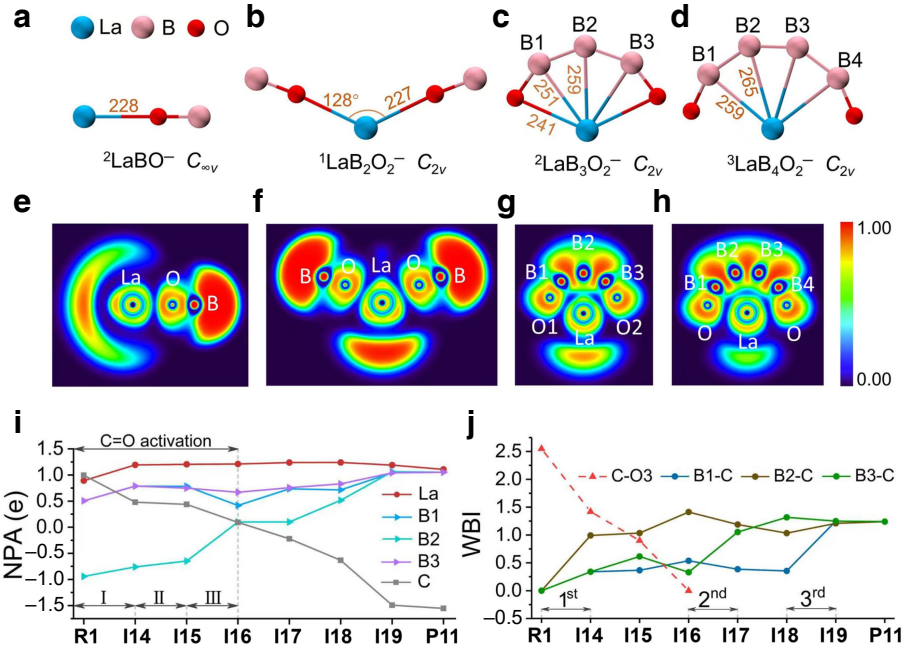

Fig. 4. Calculated global minimum structures and bonding metrics. a–d, PBE0-calculated global minimum structures: **a,** $LaBO^-$, **b,** $LaB_2O_2^-$, **c,** $LaB_3O_2^-$, **d,** $LaB_4O_2^-$ clusters, corresponding to the two-dimensional electron localization functions (ELFs) in panels (**e–h**). **i,** Natural population analysis charges along the reaction. **j,** Wiberg bond indexes for C–O3 and B–C bonds along with the reaction coordinates. The PBE0 functional, including the DFT-D3 dispersion correction, is given. The 6-311+G* basis set was selected for C and O atoms, the aug-ccPVTZ basis set was selected for the B atom, and the Stuttgart-type relativistic effective core potential basis with 28 core electrons (Stuttgart RSC ECP/ANO) was selected for the La atom. Reproduced with permission from Ref.[96], © American Chemical Society 2024.

become increasingly concentrated within the B–B bonds, which subsequently serve as electron reservoirs for CO_2 activation and conversion. Natural population analysis charges (Fig. 4i) of each atom and Wiberg bond indexes (Fig. 4j) further reveal that electron

transfer from the La atom and three B atoms to the C atom of CO_2 accompanies the first C–O bond cleavage. In this process, oppositely charged B3δ^+ and B2δ^- atoms act as a Lewis acid–base pair, cooperatively facilitating the cleavage of the C–O bond. Meanwhile, B sites effectively capture the newly formed CO moiety, thereby facilitating the formation of products containing B–C bonds. This work provided new mechanistic insights into the synthesis of organoboron compounds with multiple B–C bonds.

4 Coupling processes leading to C–N bonds

4.1 C–N bond formation via the reaction between NH_3 and CO_2

C–N bond-forming reactions represent a pivotal class of transformations, as amine derivatives are essential in numerous applications, particularly in biological and synthetic chemistry. In gas-phase studies, typical strategies for C–N bond formation from CO_2 and NH_3 or N_2 can be classified as follows: (i) reactions of metal carbide clusters with N_2 or metal nitride clusters with CO_2[97–104], and (ii) direct coupling of CO_2 with NH_3 or N_2[56–58, 105].

We reported that the reaction of $ScNH^+$ with CO_2 produces ScO^+ and isocyanic acid (HNCO) under thermal collision conditions[104]. The reaction initiates with the adsorption of CO_2 onto the positively charged Sc atom, which becomes polarized, thereby increasing the electrophilicity of the C^+ atom. Subsequently, the negatively charged N atom in $ScNH^+$ nucleophilically attacks the activated C atom via **TS1** (**Fig. 5**). This CO_2 activation mechanism can be envisaged as migratory insertion, similar to the nucleophilic attack of an amine on a polarized olefin in the condensed phase, providing a powerful method for C–N bond formation through NH_3 and unsaturated alkanes. In this reaction, the electrostatic effect is crucial for the formation of HNCO. Furthermore, previous studies showed that the reaction of Sc^+ with NH_3 yields $ScNH^+$ and H_2[106, 107]. Therefore, in light of the previously reported reaction of Sc^+ with NH_3, HNCO can be synthesized under mild conditions from NH_3 and CO_2. Further research should focus on developing catalytic systems for the atom-economical synthesis of HNCO from NH_3 and CO_2.

$$\text{Step 1}: Sc^+ + NH_3 \rightarrow ScNH^+ + H_2 \quad (1)$$

$$\text{Step 2}: ScNH^+ + CO_2 \rightarrow ScO^+ + HNCO \quad (2)$$

$$\text{Overall reaction}: Sc^+ + NH_3 + CO_2 \rightarrow ScO^+ + HNCO + H_2 \quad (3)$$

4.2 C–N bond formation via the reaction between N_2 and CO_2

In condensed-phase studies, the direct fixation of N_2 and CO_2 into value-added C–N-bonded products remains rare owing to the high kinetic barrier for activating the inert N≡N bond under mild conditions. Characteristic examples include the photolytic production of isocyanates and the electrocatalytic coupling of N_2 and CO_2 to synthesize urea[108–110]. This challenge also extends to gas-phase studies on N_2–CO_2 coupling, which are similarly very limited. To address this, we explored two strategies: plasma-assisted activation of N_2 and a purely thermal reaction pathway.

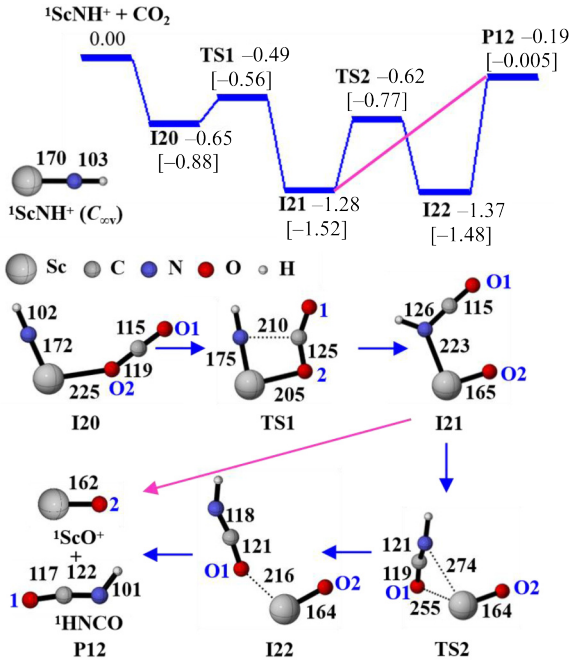

Fig. 5. Calculated potential energy surfaces for the interactions between $ScNH^+$ and CO_2, along with the corresponding Gibbs free energies at 298 K and zero-point vibrational-corrected enthalpy values ($\Delta G_{298K}/\Delta H_0$ in eV) for all reaction intermediates, transition states, and final products relative to the initial isolated reactants. The TPSS functional, including the DFT-D3 dispersion correction, is given. The 6-311+G* basis set was selected for H, C, N, and O atoms, and the def2-QZVP basis set was selected for the Cr atom. Reproduced with permission from Ref.[104]., © American Chemical Society 2019.

4.2.1 *Plasma-assisted activation of N_2*

Although plasma methods for NH_3 synthesis have been explored, their application to N_2–CO_2 coupling is novel. Crucially, plasma-induced vibrational excitation of N_2 to N_2^* dramatically lowers the N_2 activation barrier. In our study, heterobimetallic $CuNb^-$ anions were inert toward N_2 under thermal conditions, as supported by a high calculated energy barrier of +1.26 eV (**Fig. 6a**). However, in the presence of plasma, $CuNb^-$ readily captured vibrationally excited N_2^* to form $CuNbN_2^-$ ($CuNb^- + N_2 \rightarrow CuNb^- + N_2^* \rightarrow CuNbN_2^-$). This $CuNbN_2^-$ intermediate then coupled with CO_2 under thermal conditions, leading to NCO^- and NbO_2NCN^-, which contain one and two C–N bonds, respectively (Fig. 6b)[57]. We extended this research by investigating the plasma-assisted activation of N_2 and its subsequent coupling with CO_2 using a series of monometallic YB_{1-4}^- anions[105]. Under mild plasma conditions, YB_{1-4}^- can react with N_2 to form $YB_{1-4}N_2^-$ (**Fig. 7**), which can further react with CO_2 to form C–N bonds.

4.2.2 *Thermal coupling reactions of CO_2 and N_2*

The rational design of highly reactive gas-phase ions is crucial to overcoming the activation barriers for the challenging thermal coupling of CO_2 and N_2. An unprecedented direct conversion of CO_2 and N_2 into products featuring C=N bonds, including $N{=}CO^-$ and $NbO_2C{=}N^-$, by monometallic NbH_2^- was reported. According to calculations at the TPSS theory level, the most stable configuration of NbH_2^- possesses two Nb–H bonds and exhibits quintet spin multiplicity, whereas NbN_2^- is the most stable when it has two Nb–N bonds in a triplet state.

Table 3 Products, pseudo-first-order rate coefficients (k_1), reaction efficiencies (Φ), and branching ratios for the investigated CO_2–N_2 coupling reactions

	Reaction	$k1(cm^3 \cdot mol^{-1} \cdot s^{-1})$	Φ[%]	Branching ration
1	$YBN_2^- + CO_2 \rightarrow NCNBO^- + YO$	$(7.0 \pm 1.4) \times 10^{-10}$	100.3	100%
2a	$YB_2N_2^- + CO_2 \rightarrow N(BO)_2^- + YNC$	$(6.5 \pm 1.4) \times 10^{-10}$	94.5	4.8%
b	$\rightarrow YB_2N_2O^- + CO$			95.2%
3a	$YB_3N_2^- + CO_2 \rightarrow N(BO)_2^- + YBNC$	$(4.4 \pm 0.9) \times 10^{-10}$	64.5	5.4%
b	$\rightarrow YB_3N_2O^- + CO$			94.6%
4a	$YB_4N^- + CO_2 \rightarrow N(BO)_2^- + YB_2NC$	$(8.8 \pm 1.8) \times 10^{-10}$	129.5	29.9%
b	$\rightarrow YB_4N_2O^- + CO$			70.1%
5a	$CuNbN_2^- + CO_2 \rightarrow NCO^- + CuNbNO$	$(3.1 \pm 0.6) \times 10^{-9}$	96.8	29.3%
b	$\rightarrow NbO_2NCN^- + Cu$			70.7%
6a	$NbN_2^- + CO_2 \rightarrow NCO^- + NbNO$	$(5.7 \pm 1.4) \times 10^{-10}$	80.9	1.2%
b	$\rightarrow NbO_2CN^- + N$			5.8%
c	$NbO_{1-2}^- + N_2 + CO$			93%
a	$AuNbBON_2^- + CO_2 \rightarrow NCNBO^- + AuNbO_2$	$(1.8 \pm 2.1) \times 10^{-9}$	116	1.2%
b	$\rightarrow AuNbBON_2CO_2^-$			41.3%
c	$\rightarrow NbBON_2CO_2^- + Au$	—	—	25.2%
d	$\rightarrow AuNbBO_2^- + CO + N_2$	—	—	32.3%

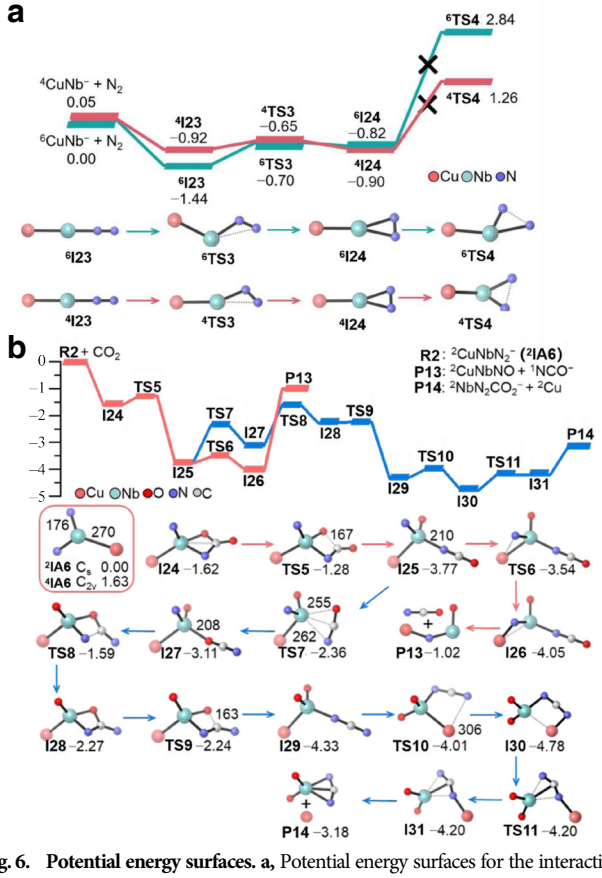

Fig. 6. Potential energy surfaces. a, Potential energy surfaces for the interaction of $CuNb^-$ with N_2. **b,** Subsequent reaction of $CuNbN_2^-$ with CO_2, along with the enthalpies corrected for zero-point vibration (ΔH_0 in eV) for relevant intermediates, transition structures, and products, relative to the isolated reactants. Spin states are denoted by superscripts. The B3LYP functional, including the DFT-D3 dispersion correction, is given. The 6-311+G* basis set was selected for C, N, and O atoms, the aug-cc-pVTZ-pp basis set was selected for the Cu atom, and the def2-TZVPD was selected for the Nb atom. Reproduced with permission from Ref.[57], © the Owner Societies 2022.

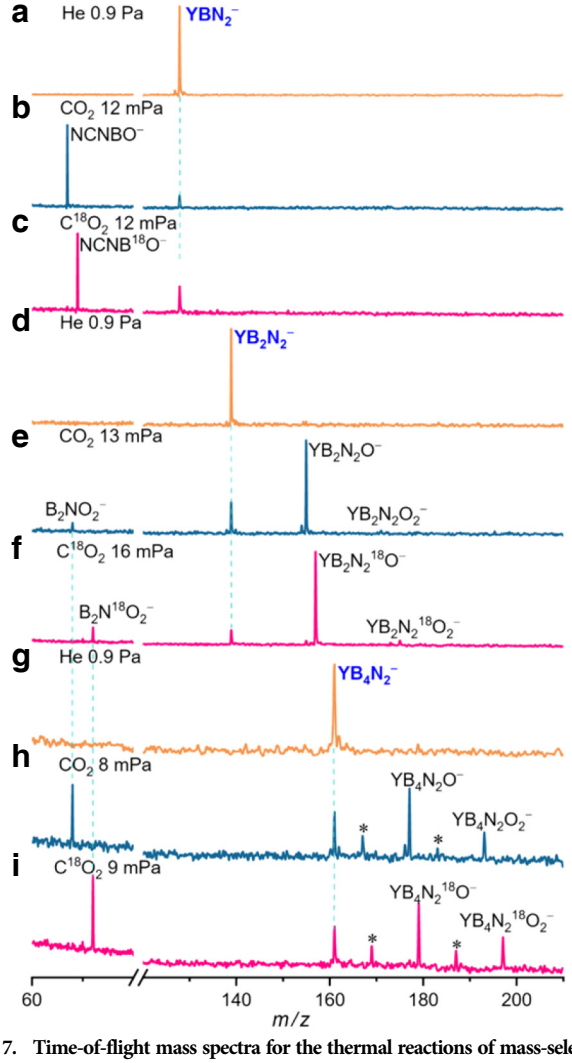

Fig. 7. Time-of-flight mass spectra for the thermal reactions of mass-selected $YB_{1,2,4}N_2^-$: (a, d, and **g)** He, **(b, e,** and **h)** CO_2, and **(c, f,** and **i)** $C^{18}O_2$. The reaction time is approximately 1.0 ms; the corresponding effective pressures of the reactant gases are indicated. Reproduced with permission from Ref.[105], © Wiley-VCH GmbH 2022.

To further study the reaction between NbH_2^- and N_2, as well as the configuration of NbN_2^-, we conducted photoelectron spectroscopy to obtain more information about the electronic structure of the generated ions (Fig. 8). The photoelectron imaging (PEI) spectra for laser ablation–generated NbN_2^- and the NbN_2^- produced from the reaction of NbH_2^- with N_2 were measured. The as-formed NbN_2^- anions are denoted as $[NNbN^-]_G$ and $[NbNN^-]_R$, respectively.

In sharp contrast, the PEI spectra obtained for NbN_2^- produced via the two aforementioned pathways display substantial differences, implying distinct structural configurations between $[NNbN^-]_G$ and $[NbNN^-]_R$. Regarding the $[NbNN^-]_R$ species, analysis of the anisotropy parameter β indicates that the initial spectral band (β = 0.33) arises from electron emission originating from orbitals of d-type character. Under 650-nm laser excitation, the experimental PEI spectrum exhibits an intense and narrow peak at 1.55 eV, along with a comparatively weaker feature near 1.60 eV. This spectral profile aligns closely with the Franck–Condon simulation for the transition from $^5\Sigma(^5$**IA9**) to $^4B_1$ (NbNN), which yields an adiabatic detachment energy of 1.44 eV. These spectral signatures can be ascribed to excitation from the SOMO1 orbital in ^{5}**IA9**, corresponding to a Nb 5d-type orbital. Therefore, the structure of NbN_2^- formed via the reaction of NbH_2^- with N_2 ($[NbNN^-]_R$) corresponds to the ^{5}**IA9** electronic configuration, rather than to that of ^{3}**IA8** or ^{1}**IA10**. In contrast, the PEI spectrum of $[NNbN^-]_G$ suggests that the experimentally observed structure produced in the ion source is ^{3}**IA8**. This means that during the reactions of NbH_2^- and N_2, N_2 was not activated; however, the bond length of the N–N bond slightly increased, consistent with preactivation. Thorough mechanistic investigations demonstrated that the most favorable reaction route for constructing a C–N bond via the coupling of CO_2 and N_2 under ambient conditions involves three main steps: (1) N_2 preactivation, (2) CO_2 activation, and (3) synchronous cleavage of N–N bonds and formation of C–N bonds.

In condensed-phase and gas-phase systems, polynuclear transition-metal complexes are conventionally employed to deliver the essential electrons that weaken or break the N≡N bond, thereby promoting chemical reactivity[111, 112], even in biological nitrogenases such as $MoFe_7S_9C$ or Fe_8S_9C[113–115]. The cooperative interplay among these metal centers, along with the presence of metal–metal multiple bonds[116], plays an important role in the adsorption and subsequent activation of N_2. This is because the participation of electrons from multiple metal atoms is necessary to back-donate into the vacant antibonding π* orbitals of N_2 for sufficiently weakening the N≡N bond. Notably, in this particular system, the activation of N_2 can be achieved with a single non-noble Nb atom, and an adjacent C atom derived from CO_2 acts as an electron reservoir, enabling both electron acceptance and donation. This interesting metal-ligand activation (MLA) approach, which involves a solitary transition-metal atom paired with one C atom, represents a completely innovative strategy for N_2 activation. The key attributes of our MLA system can be summarized as follows: (1) the active site is a single non-noble Nb atom, rather than noble metals or polynuclear metallic sites; (2) the Nb atom acts as an oxygen acceptor, with its flexible oxidation states playing a pivotal role in both the cleavage and construction of chemical bonds; (3) the C atom in CO_2 serves as an electron reservoir, facilitating the complete activation of N_2 and the formation of multiple C–N linkages. It is worth noting that H atoms play an important role in both N_2 activation and C–N coupling. For example, in N_2 activation, the H atom optimizes the electronic and steric

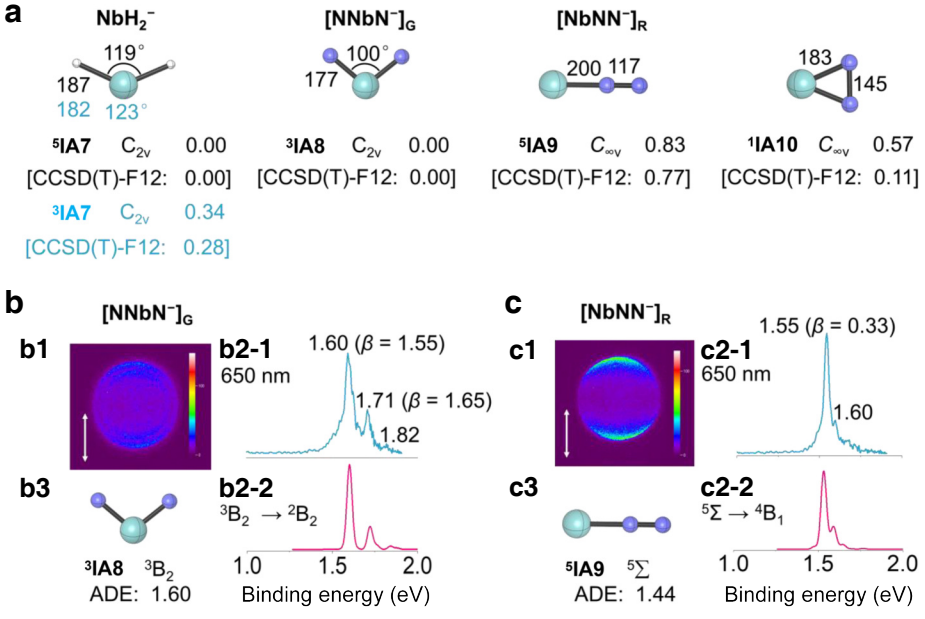

Fig. 8. The calculated structures of NbH_2^- and photoelectron images. a, The lowest-energy configurations of NbH_2^-, $[NNbN^-]_G$, and $[NbNN^-]_R$, obtained from TPSS and high-precision CCSD(T)-F12 computations, along with energies in eV, bond distances in pm, and bond angles in degrees. IA denotes the isomeric forms of the reactants NbH_2^- and NbN_2^-; **b1**, **c1,** photoelectron images (PEI), with arrows indicating the laser polarization direction; **b2-1**, **c2-1**, photoelectron spectra of $[NNbN^-]_G$ and $[NbNN^-]_R$ at a laser wavelength of 650 nm; **b2-2, c2-2** Franck–Condon simulations for the transitions corresponding to ^{3}IA8 and ^{5}IA9; **b3**, **c3**, adiabatic detachment energies for $[NNbN^-]_G$ and $[NbNN^-]_R$ calculated at the TPSS level. The TPSS functional is given. The 6-311+G* basis set was selected for H, C, N, and O atoms, the aug-cc-pVTZ-pp basis set was selected for the Cu atom, and the def2-TZVPD basis set was selected for the Nb atom. Reproduced with permission from Ref.[56], © American Chemical Society 2021.

environment of the metal center, whereas in C–N coupling, it directly participates in the key transition states via migration and proton transfer. Together, these observations highlight the unique versatility of H in N_2 fixation and C–N bond formation.

We additionally reported that $AuNbBO^-$ can directly couple relatively inert N_2 and CO_2 under thermal collision conditions, yielding $NCNBO^-$ as the product. This transformation entails the cleavage of one N≡N bond and two C=O bonds while simultaneously forming two N–C bonds. To further investigate the role of Au in the coupling of N_2 and CO_2, we mass-selected Nb_2BO^- and $NbBO^-$ clusters and examined their interactions with N_2 in an ion trap reactor. Unlike $AuNbBO^-$, Nb_2BO^- clusters display no reactivity with N_2; $NbBO^-$ can adsorb N_2 to yield $NbBON_2^-$, but the rate constant is 24 times smaller than that of the $AuNbBO^-$–N_2 system. In addition, the resultant $NbBON_2^-$ fails to react with CO_2. Frontier orbital analysis indicates that in the $AuNbBO^-$, $NbBO^-$, and Nb_2BO^- clusters, the d electrons of Nb atoms are donated to the antibonding π^* orbitals of N_2 during the formation of encounter complexes with η^1-N_2 coordination modes. For $NbBO^-$ and Nb_2BO^-, the energy gaps between d orbitals and π^* orbitals are more pronounced, which restricts the formation of Nb–N bonds (Fig. 9). In contrast, the active orbital energies of $AuNbBO^-$ are lower than those of Nb_2BO^- and $NbBO^-$, and the energy levels are more compatible with the LUMO of N_2. As a result, the introduction of Au atoms not only reduces the energies of active orbitals but also strengthens the π-back-donation interaction between $AuNbBO^-$ and N_2, which can be attributed to the matching orbital energy levels.

In brief, aside from the O atom in the $AuNbBO^-$, each of the remaining three atoms fulfills distinct and pivotal functions in the reaction process. The Nb atom acts as the adsorption site for N_2 and CO_2 molecules and is essential for breaking one C=O bond in CO_2. The Nb atom sustainably delivers electrons throughout the reaction processes involving N_2 and CO_2. During the OB–O bond formation, the B atom acts as a single-electron donor. In the following step, it accepts an activated N atom to generate a B–N bond, thereby functionalizing the N atom. The introduction of an Au atom can lower the energy levels of the active orbitals, thereby

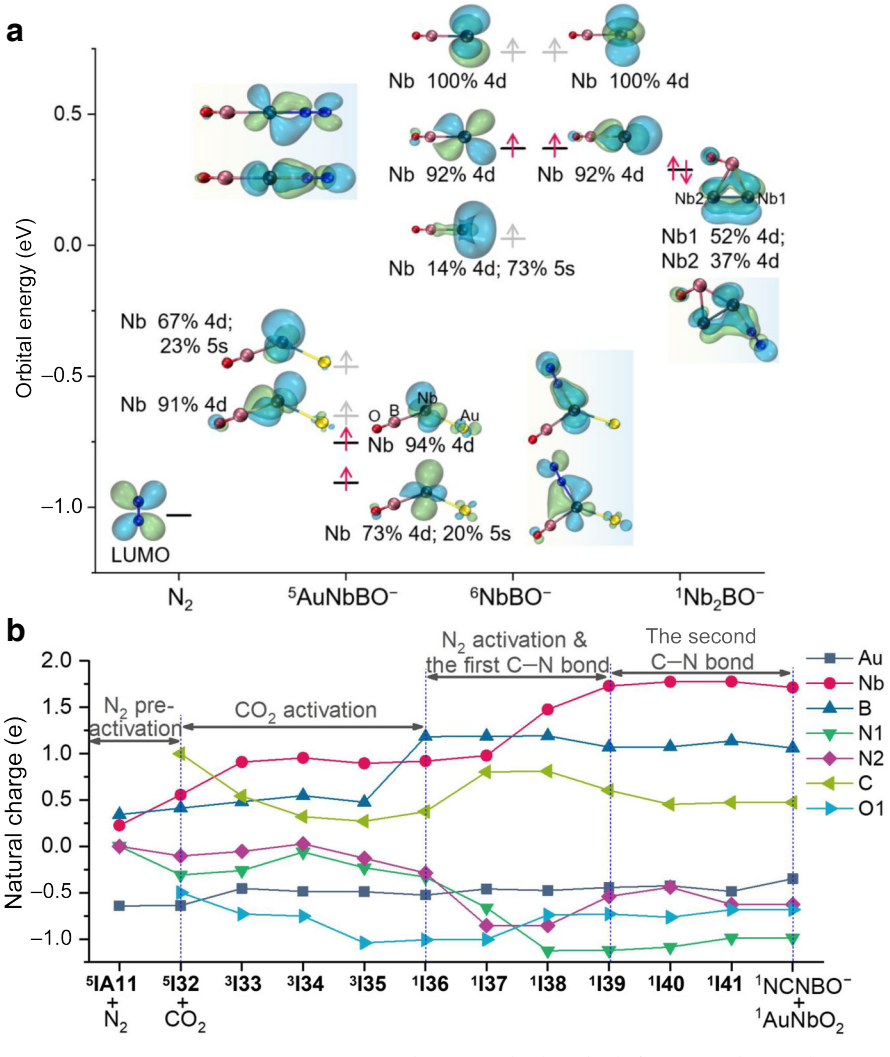

Fig. 9. Schematic molecular orbitals and Natural population analysis. a, Schematic molecular orbitals for N_2, $AuNbBO^-$, $NbBO^-$, and Nb_2BO^-, along with their compositions. The inserts display the molecular orbitals that notably interact with the π^* antibonding orbital of N_2 in $AuNbBON_2^-$, $NbBON_2^-$, and $Nb_2BON_2^-$. **b,** Natural population analysis charge distributions for each atom in the pathway for the activation of N_2 and CO_2 on $AuNbBO^-$ clusters. The B3LYP functional, including the DFT-D3 dispersion correction, is given. The 6-311+G* basis set was selected for C, N, and O atoms, the aug-cc-pVTZ-pp basis set was selected for the B atom, and def2-TZVPD was selected for the Nb atom. Reproduced with permission from Ref.[58], © American Chemical Society 2022.

facilitating the adsorption of N_2 and the subsequent reaction with CO_2. Notably, the C atom in this system sequentially captures, releases, and recaptures electrons, consistent with previous findings in the NbH_2^-–N_2–CO_2 system. In the latter, the C atom derived from the CO_2 molecule also serves as an efficient electron reservoir. The products, reaction rates and reaction efficiencies resulting from the combined reaction of carbon dioxide and nitrogen have been presented in **Table 3**.

5 Conclusions

In this review, we discussed our studies on the mechanisms of the reactions of gas-phase metal species with CO_2, combining mass spectrometry and DFT calculations. We divided CO_2 transformations into three fundamental reaction types: reduction to CO via OAT to a suitable O acceptor, B–C bond formation via reactions with metal borides, and C–N bond formation via coupling with NH_3 or N_2. However, despite advances in CO_2 activation and conversion, there are still urgent challenges to address. For instance, the formation of C_n products via C–C coupling using CO_2 molecules in the gas phase remains a great challenge. Although C–C coupling between CH_4 and CO_2 to yield C_2 products such as ketones and acetylene has been reported, the direct coupling of two CO_2 molecules or the extension of the C chain has not yet been realized. Addressing this challenge requires elucidating not only the structural nature of these sites but also the reaction mechanisms at the molecular level. Such fundamental understanding is indispensable for the rational design of catalysts with enhanced activity and selectivity.

References

[1] Qiao, J. L.; Liu, Y. Y.; Hong, F.; Zhang, J. J. A review of catalysts for the electroreduction of carbon dioxide to produce low-carbon fuels. *Chem. Soc. Rev.* **2014**, *43*, 631–675.

[2] Younas, M.; Loong Kong, L.; Bashir, M. J. K.; Nadeem, H.; Shehzad, A.; Sethupathi, S. Recent advancements, fundamental challenges, and opportunities in catalytic methanation of CO_2. *Energy Fuels* **2016**, *30*, 8815–8831.

[3] Kattel, S.; Liu, P.; Chen, J. G. Tuning selectivity of CO_2 hydrogenation reactions at the metal/oxide interface. *J. Am. Chem. Soc.* **2017**, *139*, 9739–9754.

[4] Wang, S. W.; Wang, L. G.; Wang, D. S.; Li, Y. D. Recent advances of single-atom catalysts in CO_2 conversion. *Energy Environ. Sci.* **2023**, *16*, 2759–2803.

[5] Yuan, Y. C.; Zhang, Y. H.; Li, H. Y.; Fei, M. C.; Zhang, H. N.; Santoro, J.; Wang, D. W. Methane carboxylation using electrochemically activated carbon dioxide. *Angew. Chem., Int. Ed.* **2023**, *62*, e202305568.

[6] Shi, D. X.; Feng, Y. Q.; Zhong, S. H. Photocatalytic conversion of CH_4 and CO_2 to oxygenated compounds over Cu/CdS-TiO_2/SiO_2 catalyst. *Catal. Today* **2004**, *98*, 505–509.

[7] Fors, S. A.; Malapit, C. A. Homogeneous catalysis for the conversion of CO_2, CO, CH_3OH, and CH_4 to C_{2+} chemicals via C–C bond formation. *ACS Catal.* **2023**, *13*, 4231–4249.

[8] Liu, S.; Winter, L. R.; Chen, J. G. Review of plasma-assisted catalysis for selective generation of oxygenates from CO_2 and CH_4. *ACS Catal.* **2020**, *10*, 2855–2871.

[9] Mu, B. S.; Zhang, Y. G.; Peng, M.; Tu, Z. Y.; Guo, Z. B.; Shen, S. Y.; Xu, Y.; Liang, W. Q.; Wang, X. L.; Wang, M. et al. Radiocatalytic synthesis of acetic acid from CH_4 and CO_2. *Angew. Chem., Int. Ed.* **2024**, *63*, e202407443.

[10] Khan, A.; Ansari, M. A.; Onaizi, S. A. Photocatalytic and electrocatalytic conversion of CO_2 into valuable chemicals using layered double hydroxide-based materials: A review. *Surf. Interfaces.* **2025**, *72*, 107297.

[11] Quan, Y. L.; Zhu, J. X.; Zheng, G. F. Electrocatalytic reactions for converting CO_2 to value-added products. *Small Sci.* **2021**, *1*, 2100043.

[12] Zhang, Z. Y.; Bian, L.; Tian, H.; Liu, Y.; Bando, Y.; Yamauchi, Y.; Wang, Z. L. Tailoring the surface and interface structures of copper-based catalysts for electrochemical reduction of CO_2 to ethylene and ethanol. *Small* **2022**, *18*, 2107450.

[13] Liang, S. Y.; Xiao, J. W.; Zhang, T. Y.; Zheng, Y.; Wang, Q.; Liu, B. Sulfur changes the electrochemical CO_2 reduction pathway over Cu electrocatalysts. *Angew. Chem., Int. Ed.* **2023**, *62*, e202310740.

[14] Tang, Y.; Wei, Y. C.; Wang, Z. Y.; Zhang, S. R.; Li, Y. T.; Nguyen, L.; Li, Y. X.; Zhou, Y.; Shen, W. J.; Tao, F. F. et al. Synergy of single-atom Ni_1 and Ru_1 sites on CeO_2 for dry reforming of CH_4. *J. Am. Chem. Soc.* **2019**, *141*, 7283–7293.

[15] Zhao, Y. X.; Li, Z. Y.; Yang, Y.; He, S. G. Methane activation by gas phase atomic clusters. *Acc. Chem. Res.* **2018**, *51*, 2603–2610.

[16] Ren, Y.; Yang, Y.; Zhao, Y. X.; He, S. G. Size-dependent reactivity of rhodium cluster anions toward methane. *J. Phys. Chem. C* **2019**, *123*, 17035–17042.

[17] Mou, L. H.; Jiang, G. D.; Li, Z. Y.; He, S. G. Activation of dinitrogen by gas-phase species. *Chin. J. Chem. Phys.* **2020**, *33*, 507–520.

[18] Mou, L. H.; Li, Z. Y.; He, S. G. Recent progress in dinitrogen activation by gas-phase metal species. *J. Phys. Chem. Lett.* **2022**, *13*, 4159–4169.

[19] Schwarz, H. Metal-mediated activation of carbon dioxide in the gas phase: Mechanistic insight derived from a combined experimental/computational approach. *Coord. Chem. Rev.* **2017**, *334*, 112–123.

[20] Liu, Y. Z.; Li, X. N.; He, S. G. Activation of carbon dioxide by gas-phase metal species. *Chine. J. Struc. Chem.* **2021**, *40*, 1385–1403.

[21] Wang, L. N.; Li, X. N.; He, S. G. Recent research progress in the study of catalytic co oxidation by gas phase atomic clusters. *Sci. China Mater.* **2020**, *63*, 892–902.

[22] Schwarz, H. Ménage-à-trois: Single-atom catalysis, mass spectrometry, and computational chemistry. *Catal. Sci. Technol.* **2017**, *7*, 4302–4314.

[23] Lang, S. M.; Bernhardt, T. M. Gas phase metal cluster model systems for heterogeneous catalysis. *Phys. Chem. Chem. Phys.* **2012**, *14*, 9255–9269.

[24] Gao, Y. F.; Lei, X.; Cheng, R.; Lin, S. Q.; Luo, Z. X. Enhanced stability of the $Nb_3O_6^-$ and $Nb_4O_6^+$ clusters: The *nxc*π rule versus superatomic nature. *Phys. Chem. Chem. Phys.* **2024**, *26*, 28019–28024.

[25] Gao, Y. F.; Cheng, R.; Hansen, K.; Luo, Z. X. Dual activation of CO_2 and N_2 facilitated by single Ta_4^+ clusters. *Chem. Sci.* **2026**, *17*, 2364–2371.

[26] Liu, L. J.; Lu, J. Y.; Yang, Y. H.; Ruettinger, W.; Gao, X. H.; Wang, M.; Lou, H.; Wang, Z. D.; Liu, Y. F.; Tao, X. et al. Dealuminated beta zeolite reverses Ostwald ripening for durable copper nanoparticle catalysts. *Science* **2024**, *383*, 94–101.

[27] Pastor, A.; Montilla, F.; Galindo, A. Spectroscopic and structural characterization of carbon dioxide transition metal complexes. *Adv. Organomet. Chem.* **2017**, *68*, 1–91.

[28] Dodson, L. G.; Thompson, M. C.; Weber, J. M. Characterization of intermediate oxidation states in CO_2 activation. *Annu. Rev. Phys. Chem.* **2018**, *69*, 231–252.

[29] Pérez-Jiménez, M.; Corona, H.; de la Cruz-Martínez, F.; Campos, J. Donor-acceptor activation of carbon dioxide. *Chem. -Eur. J.* **2023**, *29*, e202301428.

[30] Liu, Y. Z.; Chen, J. J.; Li, X. N.; He, S. G. Activation of carbon dioxide by $CoCD_n^-$ (n = 0–4) anions. *J. Phys. Chem. A.* **2021**, *125*, 3710–3717.

[31] He, X. Y.; Liu, Y. Z.; Wang, S. D.; Lan, X. W.; Li, X. N.; He, S. G. Multiple CO_2 reduction mediated by heteronuclear metal carbide cluster anions $RhTaC_2^-$. *Dalton Trans.* **2022**, *51*, 11491–11498.

[32] Yang, Y.; Li, Y. K.; Zhao, Y. X.; Wei, G. P.; Ren, Y.; Asmis, K. R.; He, S. G. Catalytic co-conversion of CH_4 and CO_2 mediated by rhodium-titanium oxide anions $RhTiO_2^-$. *Angew. Chem., Int. Ed.* **2021**, *60*, 13788–13792.

[33] Zhao, X. G.; Zhao, Y. X.; Liu, Q. Y.; He, S. G. Dry reforming of methane to syngas mediated by rhodium-cobalt oxide cluster anions Rh_2CoO^-. *J. Phys. Chem. Lett.* **2024**, *15*, 9167–9174.

[34] Yang, Y.; Zhang, L. J.; Wang, X. L.; Wang, R.; Zhao, Y. X.; He, S. G.; Zang, S. Q. Consecutive C–C coupling of CH_4 and CO_2 mediated by heteronuclear metal cations $CuTa^+$. *J. Am. Chem. Soc.* **2024**, *147*, 362–371.

[35] Zhao, A.; Zhao, Y. X.; Li, Q.; Zhao, X. G.; Liu, Q. Y.; He, S. G. Selective production of acetylene from the C–C coupling reaction of CH_4 with CO_2 mediated by $Ta_2O_2^+$ cluster cations. *Angew. Chem., Int. Ed.* **2025**, *64*, e202503132.

[36] Koyanagi, G. K.; Bohme, D. K. Gas-phase reactions of carbon dioxide with atomic transition-metal and main-group cations: Room-temperature kinetics and periodicities in reactivity. *J. Phys. Chem. A* **2006**, *110*, 1232–1241.

[37] Santos, M.; Michelini, M. D. C.; Lourenço, C.; Marçalo, J.; Gibson, J. K.; Oliveira, M. C. Gas-phase oxidation reactions of Ta^{2+}: Synthesis and properties of $TaO^{2+}$and TaO_2^{2+}. *J. Phys. Chem. A* **2012**, *116*, 3534–3540.

[38] Li, J. L.; Geng, C. Y.; Weiske, T.; Schwarz, H. Counter-intuitive gas-phase reactivities of $[V_2]^+$ and $[V_2O]^+$ towards CO_2 reduction: Insight from electronic structure calculations. *Angew. Chem., Int. Ed.* **2020**, *59*, 12308–12314.

[39] Armentrout, P. B.; Beauchamp, J. L. Reactions of U^+ and UO^+ with O_2, CO, CO_2, COS, CS_2 and D_2O. *Chem. Phys.* **1980**, *50*, 27–36.

[40] Sievers, M. R.; Armentrout, P. B. Gas phase activation of carbon dioxide by niobium and niobium monoxide cations. *Int. J. Mass. Spectrom.* **1998**, *179*–180, 103–115.

[41] Zhang, X. G.; Armentrout, P. B. Activation of O_2 and CO_2 by PtO^+: The thermochemistry of PtO_2^+. *J. Phys. Chem. A* **2003**, *107*, 8915–8922.

[42] Canale, V.; Robinson, R.; Zavras, A.; Khairallah, G. N.; d' Alessandro, N.; Yates, B. F.; O'Hair, R. A. J. Two spin-state reactivity in the activation and cleavage of CO_2 by $[ReO_2]^-$. *J. Phys. Chem. Lett.* **2016**, *7*, 1934–1938.

[43] Jiang, L. X.; Zhao, C. Y.; Li, X. N.; Chen, H.; He, S. G. Formation of gas-phase formate in thermal reactions of carbon dioxide with diatomic iron hydride anions. *Angew. Chem., Int. Ed.* **2017**, *56*, 4187–4191.

[44] Jiang, L. X.; Li, X. N.; He, S. G. Metal-dependent selectivity on the reactions of carbon dioxide with diatomic hydride anions MH^- (M = Co, Ni, and Cu). *J. Phys. Chem. C* **2020**, *124*, 5928–5933.

[45] Zhou, H. Y.; Wang, M.; Cui, J. T.; Sun, C. X.; Ma, J. B. The study on the reaction of gas-phase Cr_xN^- (x = 2–7) anion clusters with CO_2. *Sci. Sin. Chim.* **2020**, *50*, 1169–1176.

[46] Zhang, Y. H.; Ma, J. B. Consecutive reduction of five carbon dioxide molecules by gas-phase niobium carbide cluster anions $Nb_3C_4^-$: Unusual mechanism for enhanced reactivity by the carbon ligands. *J. Phys. Chem. A* **2024**, *128*, 2323–2329.

[47] Wesendrup, R.; Schwarz, H. Tantalum-mediated coupling of methane and carbon dioxide in the gas phase. *Angew. Chem., Int. Ed.* **1995**, *34*, 2033–2035.

[48] Firouzbakht, M.; Rijs, N. J.; González-Navarrete, P.; Schlangen, M.; Kaupp, M.; Schwarz, H. On the activation of methane and carbon dioxide by $[HTaO]^+$ and $[TaOH]^+$ in the gas phase: A mechanistic study. *Chem. -Eur. J.* **2016**, *22*, 10581–10589.

[49] Zhou, H. Y.; Wang, M.; Ding, Y. Q.; Ma, J. B. $Nb_2BN_2^-$ cluster anions reduce four carbon dioxide molecules: Reactivity enhancement by ligands. *Dalton Trans.* **2020**, *49*, 14081–14087.

[50] Zhou, S. D.; Li, J. L.; Firouzbakht, M.; Schlangen, M.; Schwarz, H. Sequential gas-phase activation of carbon dioxide and methane by $[Re(CO)_2]^+$: The sequence of events matters! *J. Am. Chem. Soc.* **2017**, *139*, 6169–6176.

[51] Rothgeb, D. W.; Hossain, E.; Mann, J. E.; Jarrold, C. C. Disparate product distributions observed in $Mo_{(3-x)}W_xO_y^-$ (x = −3; y = 3–9) reactions with D_2O and CO_2. *J. Chem. Phys.* **2010**, *132*, 064302.

[52] Yang, Y.; Yang, B.; Zhao, Y. X.; Jiang, L. X.; Li, Z. Y.; Ren, Y.; Xu, H. G.; Zheng, W. J.; He, S. G. Direct conversion of methane with carbon dioxide mediated by $RhVO_3^-$ cluster anions. *Angew. Chem., Int. Ed.* **2019**, *58*, 17287–17292.

[53] Zhao, Y. X.; Yang, B.; Li, H. F.; Zhang, Y.; Yang, Y.; Liu, Q. Y.; Xu, H. G.; Zheng, W. J.; He, S. G. Photoassisted selective steam and dry reforming of methane to syngas catalyzed by rhodium-vanadium bimetallic oxide cluster anions at room temperature. *Angew. Chem., Int. Ed.* **2020**, *59*, 21216–21223.

[54] Tang, S. Y.; Rijs, N. J.; Li, J. L.; Schlangen, M.; Schwarz, H. Ligand-controlled CO_2 activation mediated by cationic titanium hydride complexes, $[LTiH]^+$ (L = Cp_2, O). *Chem. -Eur. J.* **2015**, *21*, 8483–8490.

[55] Chen, Z. Y.; Wang, M.; Ding, Y. Q.; Ma, J. B. Two carbon dioxide molecules consecutively reduced by metal-free $B_2O_2^-$ anions. *J. Phys. Chem. A* **2023**, *127*, 3082–3087.

[56] Wang, M.; Chu, L. Y.; Li, Z. Y.; Messinis, A. M.; Ding, Y. Q.; Hu, L. R.; Ma, J. B. Dinitrogen and carbon dioxide activation to form C–N bonds at room temperature: A new mechanism revealed by experimental and theoretical studies. *J. Phys. Chem. Lett.* **2021**, *12*, 3490–3496.

[57] Chu, L. Y.; Ding, Y. Q.; Wang, M.; Ma, J. B. Plasma-promoted reactions of the heterobimetallic anions $CuNb^-$ with dinitrogen and subsequent reactions with carbon dioxide: Formation of C–N bonds. *Phys. Chem. Chem. Phys.* **2022**, *24*, 14333–14338.

[58] Ding, Y. Q.; Li, Y.; Ying, F.; Wang, M.; Ma, J. B. Room-temperature dinitrogen and carbon dioxide activation to form nitrogen-carbon bonds by quaternary cluster anions: Gold-assisted enhancement of reactivity. *J. Phys. Chem. Lett.* **2022**, *13*, 492–497.

[59] Tacey, S. A.; Jankousky, M.; Farberow, C. A. Assessing the role of surface carbon on the surface stability and reactivity of β-Mo_2C catalysts. *Appl. Surf. Sci.* **2022**, *593*, 153415.

[60] Rodriguez, J. A.; Jimenez-Orozco, C.; Flórez, E.; Viñes, F.; Illas, F. C_1 chemistry on metal carbide nanoparticles: Boosting the conversion of CO_2 and CH_4. *J. Phys. Chem. C* **2023**, *127*, 16764–16780.

[61] Liu, P.; Rodriguez, J. A. Effects of carbon on the stability and chemical performance of transition metal carbides: A density functional study. *J. Chem. Phys.* **2004**, *120*, 5414–5423.

[62] Zubarev, D. Y.; Boldyrev, A. I.; Li, J.; Zhai, H. J.; Wang, L. S. On the chemical bonding of gold in auro-boron oxide clusters Au_nBO^- (n = 1–3). *J. Phys. Chem. A* **2007**, *111*, 1648–1658.

[63] Mao, X. F.; Lu, Z. P.; Zhang, J.; Xie, Z. W. Catalyst-free regioselective diborylation of aryllithium with Tetra(*o*-tolyl)diborane(4). *Angew. Chem., Int. Ed.* **2024**, *63*, e202317614.

[64] Bisht, R.; Haldar, C.; Hassan, M. M. M.; Hoque, M. E.; Chaturvedi, J.; Chattopadhyay, B. Metal-catalysed C–H bond activation and borylation. *Chem. Soc. Rev.* **2022**, *51*, 5042–5100.

[65] Yang, J. M.; Guo, F. K.; Zhao, Y. T.; Zhang, Q.; Huang, M. Y.; Li, M. L.; Zhu, S. F.; Zhou, Q. L. Insertion of alkylidene carbenes into B–H bonds. *J. Am. Chem. Soc.* **2020**, *142*, 20924–20929.

[66] Zhao, X. M.; Jia, J.; Li, Z. Z.; Li, H. T.; Wang, Y. Q.; Wang, G. H. Stereoselective $ZnCl_2$-catalyzed B–H bond insertion of vinyl carbenes generated from cyclopropenes for the synthesis of allylboranes. *J. Org. Chem.* **2022**, *87*, 13053–13061.

[67] Hamrick, Y. M.; Van Zee, R. J.; Godbout, J. T.; Weltner, W. Jr.; Lauderdale, W. J.; Stanton, J. F.; Bartlett, R. J. The boron-carbon monoxide molecule. *J. Phys. Chem.* **1991**, *95*, 2840–2844.

[68] Burkholder, T. R.; Andrews, L. Reaction of boron atoms with carbon monoxide: Matrix infrared spectra of BCO, $(BCO)_2$, and $B(CO)_2$. *J. Phys. Chem.* **1992**, *96*, 10195–10201.

[69] Zhou, M. F.; Tsumori, N.; Li, Z. H.; Fan, K. N.; Andrews, L.; Xu, Q. OCBBCO: A neutral molecule with some boron-boron triple bond character. *J. Am. Chem. Soc.* **2002**, *124*, 12936–12937.

[70] Zhou, M. F.; Xu, Q.; Wang, Z. X.; von Ragué Schleyer, P. $B_4(CO)_2$: A new, observable σ-π diradical. *J. Am. Chem. Soc.* **2002**, *124*, 14854–14855.

[71] Zhou, M. F.; Wang, Z. X.; von Ragué Schleyer, P.; Xu, Q. Experimental and theoretical characterization of a triplet boron carbonyl compound: BBCO. *Chem. Phys. Chem.* **2003**, *4*, 763–766.

[72] Zhou, M. F.; Jiang, L.; Xu, Q. C–C double- and triple-bond formation from reactions of B atoms with CO: Experimental and theoretical characterization of OBBCCO and OBCCBO molecules in solid argon. *Chem. -Eur. J.* **2004**, *10*, 5817–5822.

[73] Jian, J. W.; Jin, J. Y.; Qu, H.; Lin, H. L.; Chen, M. H.; Wang, G. J.; Zhou, M. F.; Andrada, D. M.; Hermann, M.; Frenking, G. Observation of main-group tricarbonyls $[B(CO)_3]$ and $[C(CO)_3]^+$ featuring a tilted one-electron donor carbonyl ligand. *Chem. -Eur. J.* **2016**, *22*, 2376–2385.

[74] Zhang, Q. N.; Li, W. L.; Xu, C. Q.; Chen, M. H.; Zhou, M. F.; Li, J.; Andrada, D. M.; Frenking, G. Formation and characterization of the boron dicarbonyl complex $[B(CO)_2]^-$. *Angew. Chem., Int. Ed.* **2015**, *54*, 11078–11083.

[75] Zhou, M. F.; Kong, Q. Y.; Jin, X.; Zeng, A. H.; Chen, M. H.; Xu, Q. Infrared spectra and density functional calculations of the BCS and $B(CS)_2$ molecules in solid argon. *J. Phys. Chem. A* **2004**, *108*, 11014–11018.

[76] Jian, J. W.; Lin, H. L.; Luo, M. B.; Chen, M. H.; Zhou, M. F. Observation of spontaneous C=C bond breaking in the reaction between atomic boron and ethylene in solid neon. *Angew. Chem., Int. Ed.* **2016**, *55*, 8371–8374.

[77] Jian, J. W.; Li, W.; Wu, X.; Zhou, M. F. Double C–H bond activation of acetylene by atomic boron in forming aromatic cyclic-HBC_2BH in solid neon. *Chem. Sci.* **2017**, *8*, 4443–4449.

[78] Jian, J. W.; Wu, X.; Chen, M. H.; Zhou, M. F. Boron-mediated carbon-carbon bond cleavage and rearrangement of benzene forming the borepinyl radical and borole derivatives. *J. Am. Chem. Soc.* **2020**, *142*, 10079–10086.

[79] Cong, F.; Cai, L. Y.; Cheng, J. J.; Wang, X. F.; Andrews, L. Boron-mediated C–C and C≡N bond cleavage of acetonitrile: Matrix infrared spectra and theoretical calculations. *Organometallics* **2023**, *42*, 995–1004.

[80] Galeev, T. R.; Li, W.-L.; Romanescu, C.; Černušák, L.; Wang, L.-S.; Boldyrev, A. I. Photoelectron spectroscopy and ab initio study of boron-carbon mixed clusters: CB_9^- and $C_2B_8^-$. *J. Chem. Phys.* **2012**, *137*, 234306.

[81] Takale, B. S.; Thakore, R. R.; Etemadi-Davan, E.; Lipshutz, B. H. Recent advances in Cu-catalyzed $C(sp^3)$–Si and $C(sp^3)$–B bond formation. *Beilstein J. Org. Chem.* **2020**, *16*, 691–737.

[82] Zhao, Y.; Wang, T.; Wang, C.; Zhang, Z.; Zheng, H.; Jiang, S.; Yan, W.; Xie, H.; Li, G.; Yang, J.; et, al. Ligand-induced tuning of the electronic structure of rhombus tetraboron cluster. *ChemPhysChem* **2022**, *23*, e202200060.

[83] Deng, G. H.; Pan, S.; Dong, X. L.; Wang, G. J.; Zhao, L. L.; Zhou, M. F.; Frenking, G. Co-induced dinitrogen fixation and cleavage mediated by boron. *Chem. -Eur. J.* **2021**, *27*, 2131–2137.

[84] Deng, G. H.; Pan, S.; Jin, J. Y.; Wang, G. J.; Zhao, L. L.; Zhou, M. F.; Frenking, G. Generation and identification of the linear OCBNO and OBNCO molecules with 24 valence electrons. *Chem. -Eur. J.* **2021**, *27*, 412–418.

[85] Cook, A. K.; Schimler, S. D.; Matzger, A. J.; Sanford, M. S. Catalyst-controlled selectivity in the C–H borylation of methane and ethane. *Science* **2016**, *351*, 1421–1424.

[86] Wang, L. M.; Averkiev, B. B.; Ramilowski, J. A.; Huang, W.; Wang, L. S.; Boldyrev, A. I. Planar to linear structural transition in small boron-carbon mixed clusters: $C_xB_{5-x}^-$ (x = 1–5). *J. Am. Chem. Soc.* **2010**, *132*, 14104–14112.

[87] Averkiev, B. B.; Zubarev, D. Y.; Wang, L. M.; Huang, W.; Wang, L. S.; Boldyrev, A. I. Carbon avoids hypercoordination in CB_6^-, CB_6^{2-}, and $C_2B_5^-$ planar carbon-boron clusters. *J. Am. Chem. Soc.* **2008**, *130*, 9248–9250.

[88] Wang, L. M.; Huang, W.; Averkiev, B. B.; Boldyrev, A. I.; Wang, L. S. CB_7^-: Experimental and theoretical evidence against hypercoordinate planar carbon. *Angew. Chem., Int. Ed.* **2007**, *46*, 4550–4553.

[89] Averkiev, B. B.; Wang, L. M.; Huang, W.; Wang, L. S.; Boldyrev, A. I. Experimental and theoretical investigations of CB_8^-: Towards rational design of hypercoordinated planar chemical species. *Phys. Chem. Chem. Phys.* **2009**, *11*, 9840–9849.

[90] Galeev, T. R.; Ivanov, A. S.; Romanescu, C.; Li, W. L.; Bozhenko, K. V.; Wang, L. S.; Boldyrev, A. I. Molecular wheel to monocyclic ring transition in boron-carbon mixed clusters $C_2B_6^-$ and $C_3B_5^-$. *Phys. Chem. Chem. Phys.* **2011**, *13*, 8805–8810.

[91] Jin, J. Y.; Wang, G. J.; Zhou, M. F.; Andrada, D. M.; Hermann, M.; Frenking, G. The $[B_3(NN)_3]^+$ and $[B_3(CO)_3]^+$ complexes featuring the smallest π-aromatic species B_3^+. *Angew. Chem., Int. Ed.* **2016**, *55*, 2078–2082.

[92] Jin, J. Y.; Wang, G. J.; Zhou, M. F. Boron carbonyl analogues of hydrocarbons: An infrared photodissociation spectroscopic study of $B_3(CO)_n^+$ (n = 4–6). *J. Phys. Chem. A* **2018**, *122*, 2688–2694.

[93] Warneke, J.; Mayer, M.; Rohdenburg, M.; Ma, X.; Liu, J. K. Y.; Grellmann, M.; Debnath, S.; Azov, V. A.; Apra, E.; Young, R. P. et al. Direct functionalization of C–H bonds by electrophilic anions. *Proc. Natl. Acad. Sci. USA* **2020**, *117*, 23374–23379.

[94] Chen, Q.; Zhao, Y. X.; Jiang, L. X.; Chen, J. J.; He, S. G. Coupling of methane and carbon dioxide mediated by diatomic copper boride cations. *Angew. Chem., Int. Ed.* **2018**, *57*, 14134–14138.

[95] Chen, Q.; Jiang, L. X.; Li, H. F.; Chen, J. J.; Zhao, Y. X.; He, S. G. Thermal activation of methane by diatomic vanadium boride cations. *Acta Phys. Chim. Sin.* **2019**, *35*, 1014–1020.

[96] Zhang, F. X.; Wang, M.; Ma, J. B. Conversion of carbon dioxide into a series of $CB_xO_y^-$ compounds mediated by $LaB_{3,4}O_2^-$ anions: Synergy of the electron transfer and Lewis pair mechanisms to construct B–C bonds. *Inorg. Chem.* **2024**, *63*, 14206–14215.

[97] Li, Z. Y.; Mou, L. H.; Wei, G. P.; Ren, Y.; Zhang, M. Q.; Liu, Q. Y.; He, S. G. C–N coupling in N_2 fixation by the ditantalum carbide cluster anions $Ta_2C_4^-$. *Inorg. Chem.* **2019**, *58*, 4701–4705.

[98] Li, Z. Y.; Li, Y.; Mou, L. H.; Chen, J. J.; Liu, Q. Y.; He, S. G.; Chen, H. A facile N≡N bond cleavage by the trinuclear metal center in vanadium carbide cluster anions $V_3C_4^-$. *J. Am. Chem. Soc.* **2020**, *142*, 10747–10754.

[99] Mou, L. H.; Li, Y.; Li, Z. Y.; Liu, Q. Y.; Ren, Y.; Chen, H.; He, S. G. Dinitrogen activation and functionalization by heteronuclear metal cluster anions $FeV_2C_2^-$ at room temperature. *J. Phys. Chem. Lett.* **2020**, *11*, 9990–9994.

[100] Mou, L. H.; Li, Y.; Li, Z. Y.; Liu, Q. Y.; Chen, H.; He, S. G. Dinitrogen activation by heteronuclear metal carbide cluster anions $FeTaC_2^-$: A 5d early and 3d late transition metal strategy. *J. Am. Chem. Soc.* **2021**, *143*, 19224–19231.

[101] Mou, L. H.; Li, Y.; Wei, G. P.; Li, Z. Y.; Liu, Q. Y.; Chen, H.; He, S. G. Mutual functionalization of dinitrogen and methane mediated by heteronuclear metal cluster anions $CoTaC_2^-$. *Chem. Sci.* **2022**, *13*, 9366–9372.

[102] Li, Z. Y.; Horn, F.; Li, Y.; Mou, L. H.; Schöllkopf, W.; Chen, H.; He, S. G.; Asmis, K. R. Dinitrogen activation in the gas phase: Spectroscopic characterization of C–N coupling in the $V_3C^+ + N_2$ reaction. *Chem. -Eur. J.* **2023**, *29*, e202203384.

[103] Li, X. W.; Zhang, F. X.; Zhao, X. G.; Liu, Q. Y.; He, S. G.; Ma, J. B. Dinitrogen activation and cyanide release by the gas-phase cluster

anions $InNbC_2^-$: Synergistic effects of the p-block indium and the d-block niobium. *J. Am. Chem. Soc.* **2025**, *147*, 22185–22191.

[104] Wang, M.; Sun, C. X.; Cui, J. T.; Zhang, Y. H.; Ma, J. B. Clean and efficient transformation of CO_2 to isocyanic acid: The important role of triatomic cation $ScNH^+$. *J. Phys. Chem. A* **2019**, *123*, 5762–5767.

[105] Chen, Z. Y.; Wang, M.; Ma, J. B. Plasma-assisted coupling reactions of dinitrogen and carbon dioxide mediated by monometallic YB_{1-4}^- anions: Carbon-nitrogen bond formation. *Chem. -Eur. J.* **2022**, *28*, e202201170.

[106] Clemmer, D. E.; Sunderlin, L. S.; Armentrout, P. B. Ammonia activation by Sc^+ and Tl^+: Electronic and translational energy dependence. *J. Phys. Chem.* **1990**, *94*, 3008–3015.

[107] Russo, N.; Sicilia, E. Reaction of Sc^+ (^1D, ^3D) with H_2O, NH_3, and CH_4: A density functional study. *J. Am. Chem. Soc.* **2001**, *123*, 2588–2596.

[108] Bernskoetter, W. H.; Lobkovsky, E.; Chirik, P. J. Nitrogen-carbon bond formation from N_2 and CO_2 promoted by a hafnocene dinitrogen complex yields a substituted hydrazine. *Angew. Chem., Int. Ed.* **2007**, *46*, 2858–2861.

[109] Kayan, D. B.; Köleli, F. Simultaneous electrocatalytic reduction of dinitrogen and carbon dioxide on conducting polymer electrodes. *Appl. Catal. B: Environ.* **2016**, *181*, 88–93.

[110] Chen, C.; Zhu, X. R.; Wen, X. J.; Zhou, Y. Y.; Zhou, L.; Li, H.; Tao, L.; Li, Q. L.; Du, S. Q.; Liu, T. T. et al. Coupling N_2 and CO_2 in H_2O to synthesize urea under ambient conditions. *Nat. Chem.* **2020**, *12*, 717–724.

[111] Jia, H. P.; Quadrelli, E. A. Mechanistic aspects of dinitrogen cleavage and hydrogenation to produce ammonia in catalysis and organometallic chemistry: Relevance of metal hydride bonds and dihydrogen. *Chem. Soc. Rev.* **2014**, *43*, 547–564.

[112] Liu, J. C.; Ma, X. L.; Li, Y.; Wang, Y. G.; Xiao, H.; Li, J. Heterogeneous Fe_3 single-cluster catalyst for ammonia synthesis via an associative mechanism. *Nat. Commun.* **2018**, *9*, 1610.

[113] Sippel, D.; Einsle, O. The structure of vanadium nitrogenase reveals an unusual bridging ligand. *Nat. Chem. Biol.* **2017**, *13*, 956–960.

[114] Hoffman, B. M.; Lukoyanov, D.; Yang, Z. Y.; Dean, D. R.; Seefeldt, L. C. Mechanism of nitrogen fixation by nitrogenase: The next stage. *Chem. Rev.* **2014**, *114*, 4041–4062.

[115] Burgess, B. K.; Lowe, D. J. Mechanism of molybdenum nitrogenase. *Chem. Rev.* **1996**, *96*, 2983–3012.

[116] Zhao, Y.; Cui, J. T.; Wang, M.; Valdivielso, D. Y.; Fielicke, A.; Hu, L. R.; Cheng, X.; Liu, Q. Y.; Li, Z. Y.; He, S. G. et al. Dinitrogen fixation and reduction by $Ta_3N_3H_{0,1}^-$ cluster anions at room temperature: Hydrogen-assisted enhancement of reactivity. *J. Am. Chem. Soc.* **2019**, *141*, 12592–12600.

Data availability

Not applicable.

Acknowledgements

This work is supported by the National Natural Science Foundation of China (Nos. 22222301 and 92461313), and the Fundamental Research Funds for the Central Universities (No. 2025CX01013).

Author contributions

C. M. S.: Writing of original draft. F. X. Z. and X. W. L.: Providing data. J. B. M.: Review and editing.

Competing interests

The authors declare no competing financial interest.

Use of AI statement

None.